eng

MDPI

Article

Experimental and Numerical Investigation of the Mechanical Characteristics of Kevlar Composite Deployable Lenticular Tubes

Xinrui Wang †, Xingjian Wang, Jing Yan, Qifeng Zheng * and Junwei Sun *,†

National Key Laboratory of Automobile Chassis Integration and Bionics, School of Materials Science and Engineering, Jilin University, Changchun 130022, China

* Correspondence: zhengqf@jlu.edu.cn (Q.Z.); sunjunwei1125@gmail.com (J.S.)

† These authors contributed equally to this work.

Abstract

Carbon fiber-reinforced plastics (CFRP) are widely used in deployable space structures due to their strength-to-weight ratio, yet their inherent brittleness and limited damage tolerance constrain their performance under large deformation. This study reports a new concept, the Kevlar composite deployable lenticular tube (CDLT), for improved toughness and reliable stowability. The buckling response of Kevlar CDLT under axial compression and torsion was characterized, and its stowability was verified through experiments and finite element analysis (FEA). Axial compression studies show that the load–displacement curve transitions from linear elastic to nonlinear deformation at the critical buckling load; meanwhile, local stress magnification occurs in the central arc region. Damage analysis further reveals that buckling instantaneously induces localized wrinkling and matrix failure. Torsional analysis shows that the CDLT exhibits an initially linear torque–twist response, governed by shear stiffness. However, once the critical torque is exceeded, torque decreases sharply due to localized collapse and overall buckling. Moreover, the outermost layers bear the highest stresses, whereas the inner layers remain comparatively uniform and less stressed. Furthermore, the influence of different layup sequences, ply numbers, and total thickness on the load-bearing capacities of CDLT was investigated, ultimately determining the optimal layup scheme. Finally, the stowability analysis demonstrates that the Kevlar CDLT, configured as a six-ply laminate with a total thickness of 0.72 mm, achieves an optimal balance between stiffness and flexibility. In this comparison, both the Kevlar and CFRP CDLTs employ identical lenticular cross-sectional geometries, fully consistent boundary conditions, the same overall laminate thickness (0.72 mm), and an identical stacking sequence of [45°/−45°/90°/90°/45°/−45°], with the material properties being the only variable. Under these strictly controlled conditions, the coiling torque of the Kevlar CDLT is reduced by at least 48% relative to that of the CFRP CDLT. This study preliminarily verifies the load-bearing capacity and stowability of novel Kevlar CDLTs, providing valuable guidance for the design of deployable space structures.

Keywords: composite deployable lenticular tubes; buckling behavior; axial compression; torsion; finite element analysis

Check for updates

Academic Editor: Masami Okamoto

Received: 13 January 2026
Revised: 1 February 2026
Accepted: 6 February 2026
Published: 18 February 2026

Copyright: © 2026 by the authors. Licensee MDPI, Basel, Switzerland. This article is an open access article distributed under the terms and conditions of the Creative Commons Attribution (CC BY) license.

1. Introduction

In recent years, deployable structures have attracted increasing attention in aerospace engineering due to their excellent structural performance, including high strength and stiffness, high dimensional stability, compactness, and lightweight design [1–3]. According

to the geometric cross-section profiles, deployable structures in space applications can be generally classified as open-section and closed-section ones [4–7]. In particular, the Storable Tubular Extendable Member (STEM) [8,9], tape-spring hinges [10], the Triangular Retractable and Collapsible (TRAC) boom [11], C-shaped tubes [12,13], and Collapsible Tubular Mast (CTM) [14] have been studied for their folding responses, buckling behaviors, and deployment mechanics. Among them, deployable composite lenticular tubes (CDLT) have attracted much attention for their high +packaging efficiency and excellent deployment performance, and show strong potential for horizon applications in aerospace [15,16]. NASA and ESA have successfully developed and validated multiple lens-arm-based solar sails [17,18], which have demonstrated reliable deployment and retraction capabilities.

Space deployable structures in the early age used materials with high specific strength, toughness, and low thermal expansion coefficient, such as Cu-Be or steel [19,20]. Adeli designed a prismatic folding boom made of copper–beryllium to build a solar sail support boom for CubeSail with a fully deployed length up to 3.6 m [21]. Afterwards, ESA researchers conducted stiffness and load tests on the deployment arm within the Gossamer satellite deorbiting project [22]. Even though metals offer known advantages in manufacturing processes and high specific stiffness, their disadvantages include high density, fatigue susceptibility, and significant thermal deformation, which limit their further development for space-deployable structures. In contrast, fiber-reinforced composites are able to achieve exceptional specific strength and stiffness, tunable anisotropy, and superior fatigue resistance via inclusion of high-strength fibers in a polymer matrix [23,24]. Against this backdrop, carbon fiber-reinforced polymer (CFRP) has emerged as a key material for lenticular deployable space structures [25]. NASA and JAXA have designed and tested several types of CFRP deployable booms for solar sails and antennas [26,27]. Additionally, Sun et al. [14] designed and optimized the CDLT structure based on stress conditions during compression and folding processes, maximizing material efficiency while being lightweight. Chen et al. [7] analyzed the flattening, stretching, coiling, and deployment of thin-walled carbon fiber composite CDLTs using axial buckling and modal analysis. Other studies also reported the influence of layup sequence [28], curing-induced distortion [29], and vibration properties [30] on the performance of CFRP CDLTs. However, carbon fiber composites are prone to brittleness and accelerated microcrack propagation under thermal cycling and micrometeoroid impacts, which severely limit their long-term durability in deployable space structures [31].

On the contrary, extensive studies have demonstrated that aramid (Kevlar) reinforced fiber composite (ARFP) offers a unique and optimal combination of high specific strength, low density, thermal stability, and impact resistance. NASA's MMOD shielding heritage provides strong evidence: Kevlar fabrics are widely adopted in the Stuffed Whipple shields of the International Space Station, where the material serves as the primary high-strength component in inner bumper layers due to its excellent ability to arrest and dissipate hypervelocity debris clouds [32]. Flight-proven systems, such as those on the ISS, ESA Columbus, PMM, and ATV, all rely on Kevlar to achieve high-performance shielding while significantly reducing mass relative to all-metal designs [33]. Beyond protection systems, Kevlar plays a critical role in deployable and inflatable space structures, where low mass, flexibility, and high strength are essential. Numerous studies have shown that Kevlar-reinforced inflatable booms exhibit reliable deployment behavior and stable structural performance in orbit, with experiments confirming their ability to maintain shape accuracy and load-bearing capacity [34]. Taken together, these qualities highlight Kevlar's considerable promise as an enabling material for deployable space structures.

Although Kevlar composites have shown clear advantages in aerospace structures, their mechanical properties within deployable structures remain insufficiently understood.

Previous research has mainly focused on Kevlar shielding and inflatable membranes, with scant investigation into the load-bearing capacity and stowability of Kevlar space deployable structures. However, as modern space missions pursue lighter, more compact deployable structures, these issues are becoming increasingly important. To address this gap, the present study focuses on investigating the load-bearing capacity of Kevlar CDLTs, particularly their axial compression and torsional buckling behaviors. Additionally, by integrating experimental testing with FEA, we evaluated the influence of laminate thickness, ply number, and layup sequence on load-bearing performance. Further, we assessed how layer thickness influences coiling performance. The results systematically elucidate the load-bearing and deformation characteristics of Kevlar CDLT, offering practical guidance for designing Kevlar-based deployable structures that are both lightweight and mechanically reliable.

This paper is organized as follows: Section 2 describes specimen preparation and the experimental procedures for axial compression and torsion tests. Section 3 presents the evolution of displacement versus critical buckling load, the distribution of strain and damage in axial compression, and the torque–torsion relationship based on experimental and simulation studies. Section 4 investigates the influence of parameters on specimen buckling behavior. Section 5 verifies the stowability of Kevlar CDLT by combining coiling experiments with FE simulations and comparing it with carbon fiber materials, and Section 5 concludes the study.

2. Preparation and Experiments

2.1. Material and Specimen

The CDLT specimen was fabricated from Kevlar-29/epoxy composite prepregs supplied by DuPont (United North Road 215, Fengxian District, Shanghai, China). Figure 1 shows the geometric parameters and cross-sectional profile of the ultra-thin-walled CDLT [14]. The cross-section can be idealized as two identical Ω-shaped shells. Each shell consists of three tangential arc segments, with two horizontal bonding interfaces of 5 mm width. A stacking sequence of [90°/0°/90°/0°/90°/0°] was used by CDLT; all layer angles referenced herein denote the angle between the warp yarn and the horizontal direction or the +X axis, with each layer being 0.12 mm thick and the total length of the sequence being 700 mm. The sequence comprised six layers.

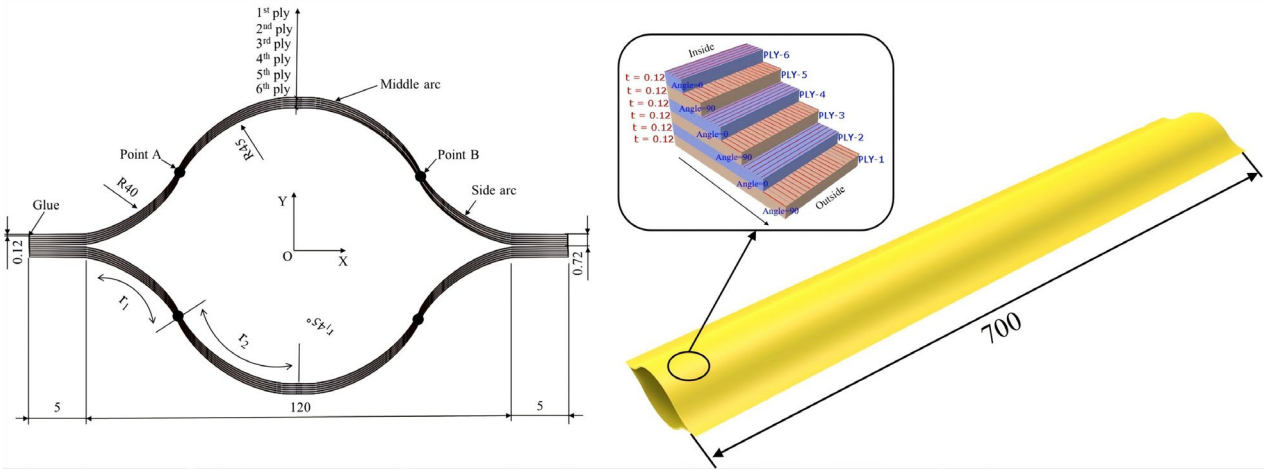


Figure 1. Geometrical dimension and FE model of CDLT cross-section.

The structure was fabricated using a vacuum bag curing process. Table 1 summarizes the specifications and performance parameters of the Kevlar-29/epoxy composite. As shown in Figure 2a, the manufacturing process comprises three stages: (1) Layup and

vacuum-bag encapsulation: prepregs with different fiber angles were cut into rectangles of 150 × 700 mm^2 and then stacked and compacted in a specific order. Release paper and resin-absorbing felt were laid over the prepreg to promote resin flow, which aids in uniform curing and reduces surface defects. Finally, the assembly was vacuum-bagged and sealed with vacuum tape to ensure airtight consolidation during curing. (2) Vacuum bag curing stage: rapid vacuum extraction prevents wrinkling or defects. The curing cycle was provided by the manufacturer (Figure 2b), including heating at a rate of 0.75 °C/min to 70 °C followed by an isothermal curing stage of 40 min, then heating at the same rate to 100 °C with an isothermal curing stage of 1.5 h, and finally cooling to room temperature under a constant pressure of 0.2 MPa. (3) Bonding interface bonding stage: after demolding, the CDLT specimens were trimmed and carefully ground to achieve the designed dimensions. Subsequently, the two shells were bonded together along the bonding interfaces using a laboratory-fabricated bonding film. C-clamps were applied at the bonding region to ensure accurate alignment of the two shells during assembly. An aluminum inner mold was placed inside the hollow section to prevent undesired deformation during the subsequent heating process. Finally, the assembled component was transferred to an oven and subjected to secondary thermal cycling to complete the adhesive curing.

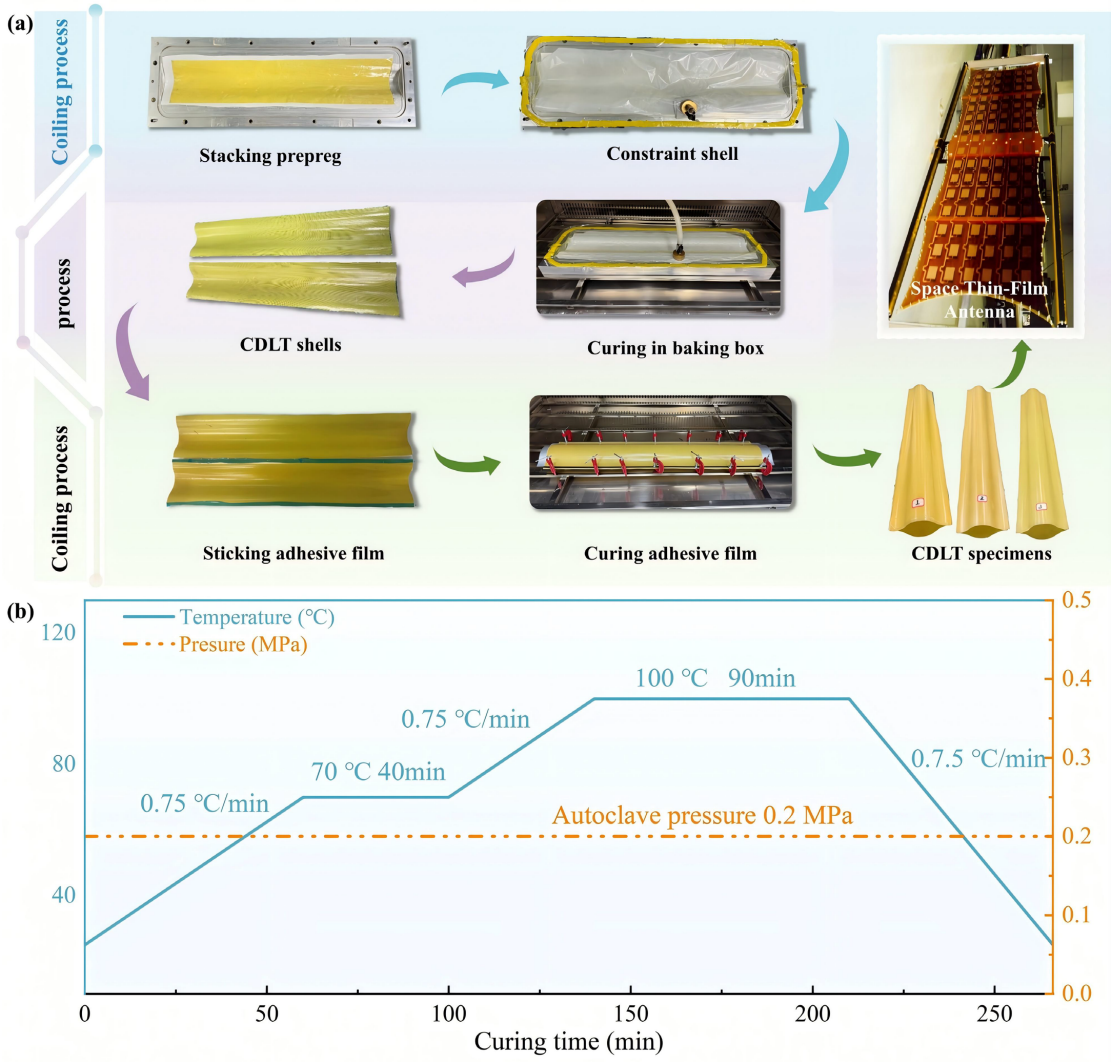


Figure 2. Preparation of the CDLT specimens: (**a**) preparation process and (**b**) curing process temperature curve.

Table 1. Material parameters of the Kevlar-29/Epoxy composite [35].

Parameter	Notation	Values
Density	ρ (kg/m^3)	1259
Young's modulus in direction 1	E_1 (GPa)	20.5
Young's modulus in direction 2	E_2 (GPa)	20.5
Young's modulus in direction 3	E_3 (GPa)	6.0
Poisson's ratio in direction 12	v_{12}	0.21
Poisson's ratio in direction 13	v_{13}	0.33
Poisson's ratio in direction 23	v_{23}	0.33
Shear modulus in direction 12	G_{12} (GPa)	0.77
Shear modulus in direction 13	G_{13} (GPa)	2.71
Shear modulus in direction 23	G_{23} (GPa)	2.71
Tensile strength in direction 1	X_{1t} (GPa)	0.595
Compressive strength in direction 1	X_{1c} (GPa)	0.595
Tensile strength in direction 2	X_{2t} (GPa)	0.595
Compressive strength in direction 2	X_{2c} (GPa)	0.595
Shear strength in direction 12	S_{12} (GPa)	0.077
Shear strength in direction 13	S_{13} (GPa)	0.54
Shear strength in direction 23	S_{23} (GPa)	0.54
Failure equivalent strain	*Fs*	0.2

2.2. Buckling Test

In aerospace systems, such as solar sail missions, CDLTs are used as the primary load-carrier structure. Their deployment stability is critical to overall structural reliability, but the combination of high slenderness ratios and dynamic loads often leads to instability. Such instability may manifest as buckling under axial compression or torsional loading, which may compromise structural integrity.

For experimental reliability, three of the same size CDLT specimens were prepared for an average result value. All the specimens were six-layer Kevlar laminates with a laminate orientation of [90°/0°/90°/0°/90°/0°], and their dimensions and material properties are shown in Section 2.1. The experiments were performed under quasi-static loading conditions using an AGX-100 kN servo-hydraulic testing machine manufactured by Shimadzu Corporation (Kyoto, Japan). The measurements were carried out under dry conditions at room temperature. The displacement rate was 2 mm/min, and the maximum compression displacement was 2.5 mm. Figure 3a shows the complete test setup, including the fixture and the loading device. Strain gauges were used to measure local deformation and the axial strain response as the compression test was conducted. As shown in Figure 3b, these gauges were equally distributed along the centerline of longitudinal upper and lower shells with a spacing of 100 mm to measure strains at six sections (100–600 mm). Shielded cables connected to the DH3816 static strain acquisition system, ensuring stable signal transmission and high-fidelity load–displacement data.

Apart from compressive loads, the deployment may also be subject to twisting loads caused by structural vibration or disturbances in the environment. A specialized torsion test setup is shown in Figure 3c, with a custom torsion model to sense torque finely. Application and measurement of the torque is facilitated with a DIP-1000 static torque transducer (precision: $\pm$0.01 N m) in which the specimen is clamped using rigid metallic supports; lentil-shaped metallic inserts provide proper width dimensions of the sample inside the cross-section structure. One end connects to the torque sensor, and the other end is attached to a turning machine for fine angular movement. The sensor can also be used for online torque detection with a computer-controlled data acquisition system.

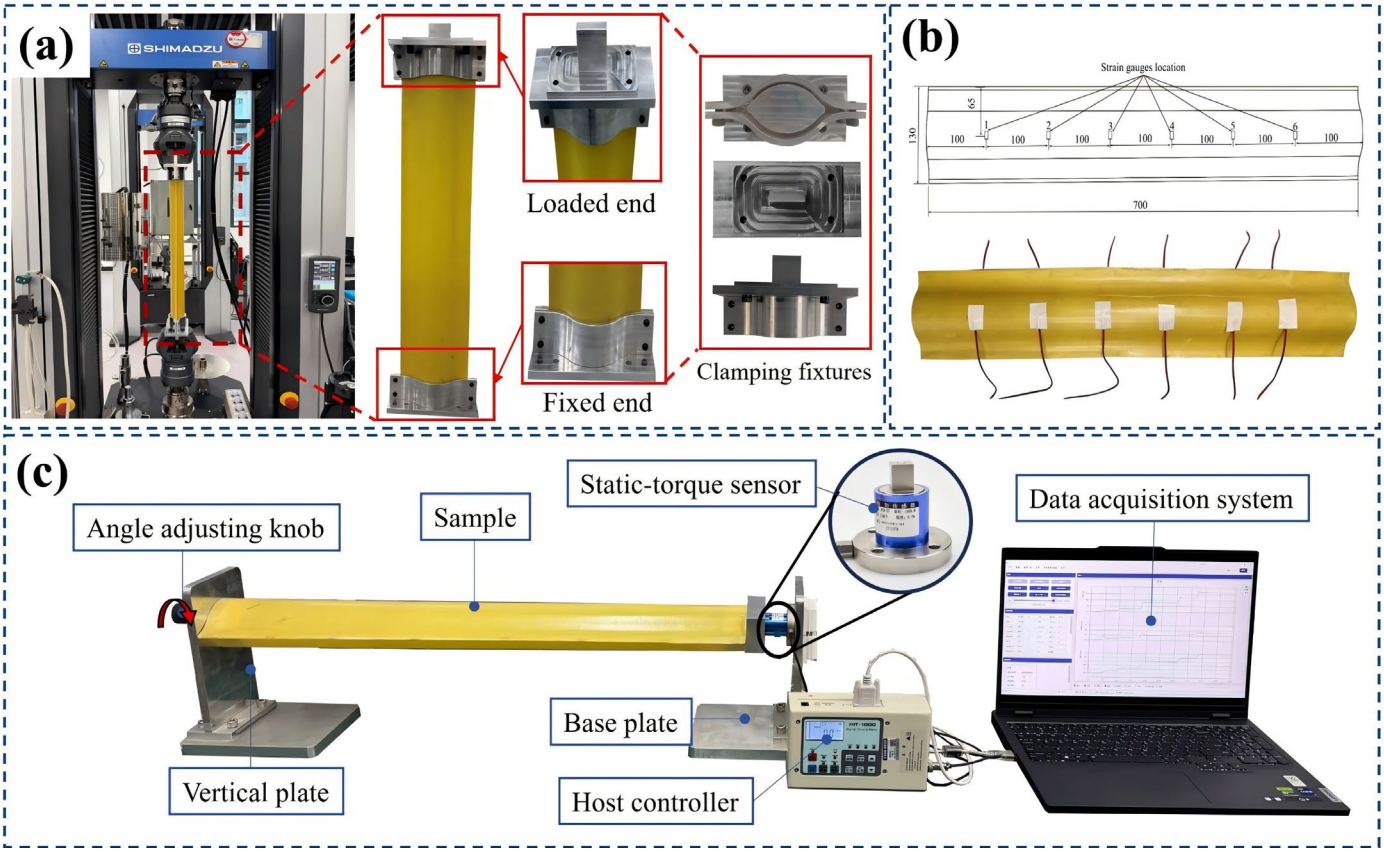


Figure 3. Experiments on CDLT buckling behaviors: (**a**) compressive loading experiment and boundary condition of CDLT specimen in tests; (**b**) sensor arrangement locations for compressive test; (**c**) torsion device.

3. Finite Element Simulation

3.1. FE Models

Based on the experimental boundary and load conditions described in Section 2.2, FE models of the axial compression and torsion of the CDLT were established, as shown in Figure 4a, to analyze their buckling behavior. The fixture material model uses a modulus of elasticity of 210 GPa, a density of 7800 kg·m^{-3}, and a Poisson's ratio of 0.3. The CDLT shells are discretized using four-node hyperbolic shell elements (S4R), which incorporate hourglass control and six degrees of freedom per node. Furthermore, the adhesive layer between the upper and lower shells is modeled with cohesive elements. Previous studies confirm that these elements accurately capture the nonlinear deformation and post-buckling response of thin composite shells, particularly for problems involving finite membrane strain and large rotation angles. Mesh sensitivity analysis showed that additional refinement yielded only marginal convergence gains while substantially increasing computational time, so a 3 mm mesh was selected as the optimal compromise between accuracy and efficiency. Detailed mesh sensitivity analysis is provided in the Supporting Materials S1.

Axial compression buckling model: The boundary conditions employed in the experiment were reconstructed in the FE model using the reference point coupling method within the "Interactive" module. The fixed-end reference point was fully constrained in all translational and rotational degrees of freedom, while the loaded end was permitted translational movement only along the compression axis. To ensure consistency with the experimental loading rate of 2 mm/min, an explicit dynamic solver applied a 2.5 mm displacement-controlled load to capture post-buckling evolution, as shown in Figure 4b. This setup enabled the simulation to resolve the nonlinear coupling between stiffness

degradation and buckling initiation. To ensure computational accuracy, mass scaling was not applied. By monitoring the ratio of kinetic to internal energy, as shown in Figure 5a, the quasi-static nature of the analysis was verified—this ratio remained below 5% throughout the entire loading process.

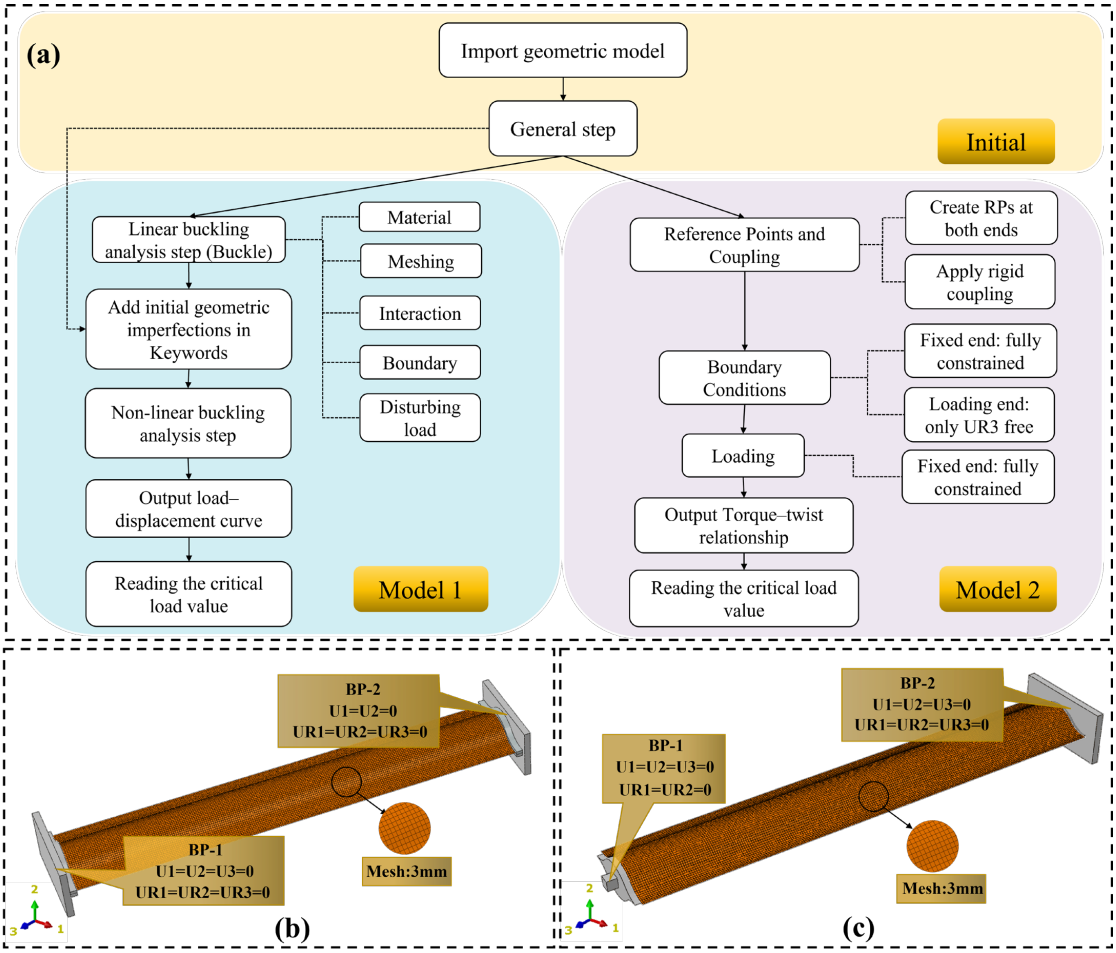


Figure 4. Buckling behavior of the CDLT predicted by FEA model: (**a**) flow chart of the simulation process; (**b**) axial compression boundary condition and mesh density; (**c**) torsion boundary condition and mesh density.

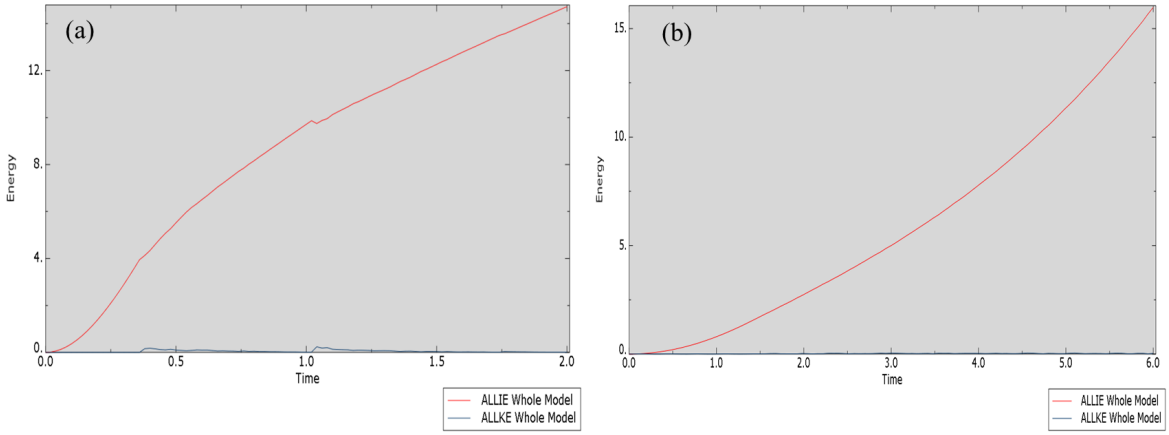


Figure 5. Ratio of kinetic energy to internal energy in buckling finite element analysis: (**a**) ratio of kinetic energy to internal energy in axial compression; (**b**) the ratio of rotational kinetic energy to internal energy.

Torsional buckling model: Boundary and load conditions for the torsional simulation are implemented via reference point coupling. This approach is analogous to the compression model. Reference point 1 is coupled to the active-end node. Reference point 2 is coupled to the fixed-end node. As shown in Figure 4c, torsional loading is introduced by applying a controlled rotation between the two reference points. Reference point 1 restricts translation in all directions (U1 = U2 = U3 = 0) while allowing rotation only around the load axis (UR1 = UR2 = 0). Reference point 2 is fully constrained (U1 = U2 = U3 = 0; UR1 = UR2 = UR3 = 0). A rotation of 30° was applied within an analysis step time of 6 s. The quasi-static condition was confirmed by monitoring the kinetic-to-internal energy ratio, which consistently remained below 5% during the entire loading process (Figure 5b).

The Hashin failure criterion is included within the simulation framework as a primary failure model of fiber-reinforced composites to study post-buckling damage evolution. For laminated composite structures modeled with shell elements, the Hashin criterion is widely adopted due to its capability to distinguish fiber-dominated and matrix-dominated failure modes under both tensile and compressive loading. This method model defines four different types of independent damage modes—fiber tension, fiber compression, matrix tension, and matrix compression—associated with the constitutive relations of Equations (1)–(4):

Tensile failure of fibers:

$$\left(\frac{\sigma_1}{X_T}\right)^2 + \left(\frac{\tau_{12}}{S_L}\right)^2 = 1, \sigma_1 \geq 0 \tag{1}$$

Tensile failure of fibers:

$$\left(\frac{\sigma_1}{X_C}\right)^2 = 1, \sigma_1 < 0 \tag{2}$$

Tensile failure of resin:

$$\left(\frac{\sigma_2}{Y_T}\right)^2 + \left(\frac{\tau_{12}}{S_L}\right)^2 = 1, \sigma_2 \geq 0 \tag{3}$$

Compressive failure of resin:

$$\left[\left(\frac{Y_C}{2S_T}\right)^2 - 1\right]\frac{\sigma_2}{Y_C} + \left(\frac{\sigma_2}{2S_T}\right)^2 + \left(\frac{\tau_{12}}{S_L}\right)^2 = 1, \sigma_2 \leq 0 \tag{4}$$

In the Hashin failure criterion, σ_1 and σ_2 represent stresses along the fiber direction and transverse direction, respectively, while τ_{12} denotes the in-plane shear stress acting along the 1–2 material axis. X_T and X_C denote the tensile strength and compressive strength of the fiber, respectively, while Y_T and Y_C correspond to the tensile strength and compressive strength of the matrix. S_L and S_T represent the longitudinal shear strength and transverse shear strength, respectively.

3.2. Numerical Study on Axial Buckling and Failure Behavior

Due to their lightweight and thin-shell characteristics, CDLTs are prone to vibration under dynamic loading; thus, identifying their natural frequencies and mode shapes is essential for ensuring deployment stability. Under free boundary conditions (Figure 6a), the first six modes represent rigid-body motions, while the seventh to tenth modes (295.16–306.85 Hz) exhibit localized breathing deformation either at the ends or along the mid-section. Here, the breathing deformation refers to a symmetric radial expansion and contraction of the lenticular cross-section, characterized by in-plane shell deformation rather than global bending or torsional motion. For cantilevered conditions (Figure 6b), the

first four natural frequencies are 58.03, 135.44, 155.42, and 227.61 Hz, with the first mode showing global bending and higher modes displaying breathing deformation near the free end. These cantilevered modes, derived from the free-state patterns but frequency-shifted by constraints, provide critical mode shapes for introducing initial imperfections in buckling analyses. The first three linear buckling modes (Figure 6c) indicate breathing-type deformation along the bonded edges and curved arc, with higher modes showing additional localized corrugations. The corresponding buckling eigenvalues are 3058.3, 3275.3, and 3272.9. According to Equation (5), the predicted linear critical load is much larger than the experimental value of 2154.8 N, highlighting the limitations of linear eigenvalue buckling analysis in capturing the actual failure load of defect-sensitive shells.

$$P_{cr} = \lambda P = 3275.3 \times 1\ \text{N} = 3275.3\ \text{N} \tag{5}$$

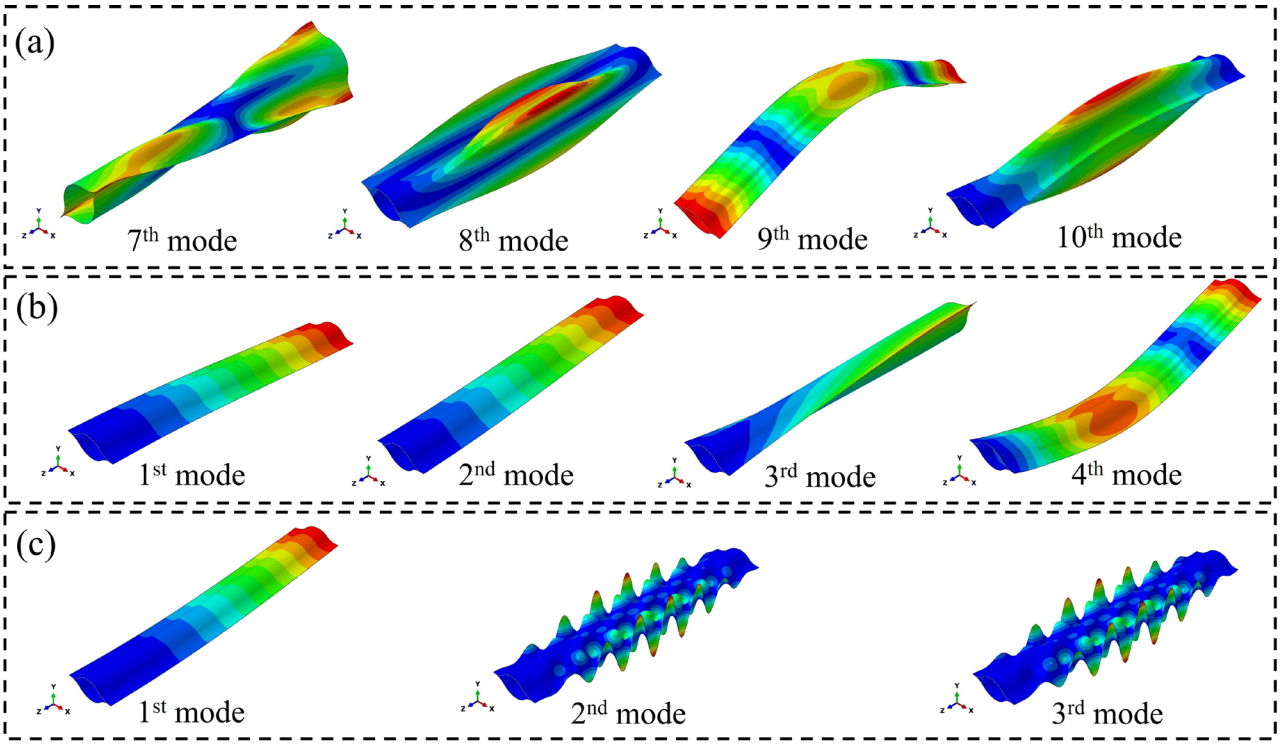


Figure 6. (**a**) Mode shapes of CDLTs in free vibration; (**b**) mode shapes of CDLTs in cantilever vibration; (**c**) first three mode shapes in linear buckling.

Therefore, nonlinear buckling analysis is essential for evaluating the actual load-carrying capacity of CDLTs. To ensure that simulations match the tested specimen, measured imperfections were introduced using ABAQUS's "IMPERFECTION" keyword in the nonlinear buckling analysis. The defect amplitude was scaled by the coefficient a, which adjusts the initial defect magnitude. The linear buckling mode was then multiplied by a to create the imperfect geometry needed for nonlinear analysis under axial compression. Since the first mode of vibration governs the minimum buckling load, it was used as the primary defect mode. To improve accuracy, the first two modes were combined in a 2:1 amplitude ratio, resulting in a normalized defect amplitude of 0.9 [30].

To determine the mechanical properties and geometric nonlinear behavior of CDLTs under compressive deformation, compression tests were performed, as detailed in Section 2.2. The load–displacement curves are presented in Figure 7, which were obtained experimentally and via FE simulations. In the initial stage, CDLT specimens display a linear elastic behavior in which the load increases nearly proportionally with displace-

ment. The load reaches a maximum of 2154.8 N at a displacement of 1.44 mm, after which the stiffness decreases quickly and the curve almost immediately collapses as buckling instability occurs. This phenomenon is a hallmark of shell buckling: once the critical load is reached, the structure deforms into a buckled configuration and loses its load-bearing capacity. These results indicate that the numerical simulation successfully captures the overall buckling behavior and deformation characteristics observed in the experiments. Nevertheless, the predicted buckling load is higher than the experimental value. This overestimation is primarily attributed to the idealized assumptions adopted in the finite element model, including perfect geometric configuration, uniform material properties, and ideal boundary conditions. In contrast, the experimental specimens inevitably contain initial geometric imperfections, manufacturing-induced variability, and slight compliance at the loading interfaces, which tend to reduce the measured buckling load. Despite this discrepancy in peak load, the post-buckling deformation mode and the overall trend of the load–displacement response show good qualitative agreement between the numerical and experimental results.

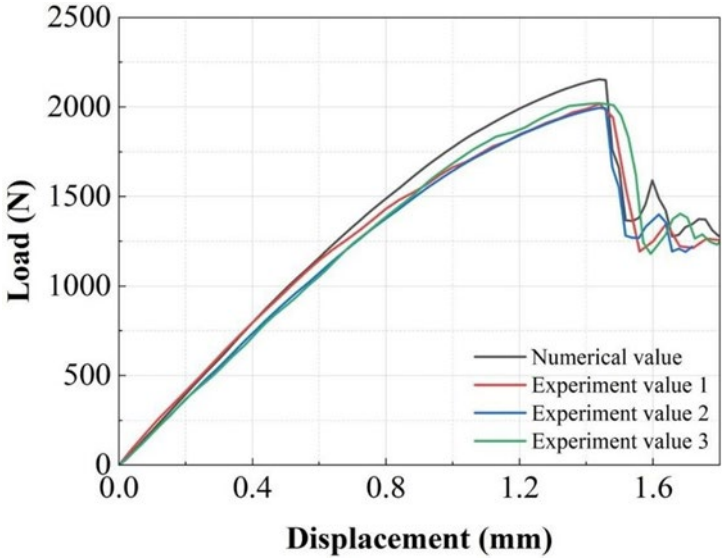


Figure 7. Comparison of numerical and experimental load–displacement relationships.

To further explain the local deformation mechanism of CDLTs, two representative stress–strain paths, Path 1 and Path 2, were defined for detailed strain analysis (Figure 8a). Path 1 follows the centerline of the central arc, and Path 2 is at a lateral position of 325 mm from the fixed end. Figure 8b shows strain curves from gauges used during the axial compression test in Section 2.2. The results indicate that strain values increase continuously with compressive displacement. Strain values peak in the central 300–400 mm region. Gauges symmetrically positioned along the transverse axis show similar patterns, indicating symmetrical deformation at these locations. Finite element numerical strain states, under compression loads of 0.7 kN, 1.4 kN, and 2.1 kN (Figure 8c), further support the strain observations from the experiments. At low loads, strain along the tube's length is relatively uniform and gradual. When the load increases to 2.1 kN, localized strain intensifies, forming a strong compressive strain gradient between 200 mm and 400 mm from the tube end. To further examine the stress condition in this critical region, axial compressive stresses in each laminate ply were extracted along Path 2 (Figure 8d). The middle plies bear the lowest stresses, whereas stresses gradually increase toward the outer plies. The outermost ply experiences the highest stress due to bending-induced variation across the laminate thickness. Interlaminar stresses remain low, but a pronounced stress

concentration develops in the arc region, consistent with the experimentally identified buckling and collapse zone. This confirms that the central arc is the primary instability region under axial compression.

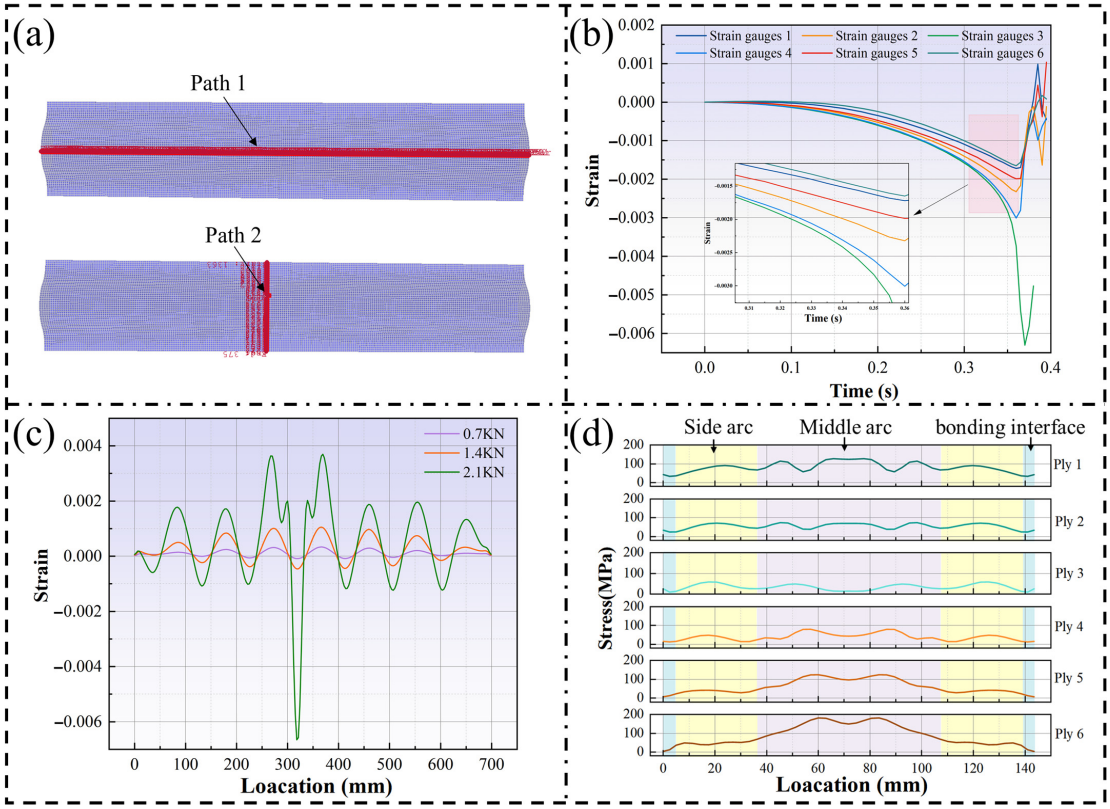


Figure 8. Stress–strain distribution of CDLT under axial compression: (**a**) strain path definition; (**b**) strain distribution at different strain gauge locations; (**c**) strain distribution under different stresses; (**d**) stress distribution under different numbers of layers.

The axial compression experiments also show that buckling of the CDLT occurs via local collapse and wrinkle formation in the central arc (Figure 9a), matching the deformation pattern predicted by the numerical results. With increasing load, the Hashin failure index rapidly approaches the critical threshold, signaling the initiation of matrix compression damage (Figure 9b). This failure mode is mainly attributed to local shell instability, which produces high transverse stress and results in cracking of the epoxy matrix. The Kevlar fibers remain undamaged due to their high toughness and continue to sustain load even after matrix degradation begins.

3.3. Torsion Behavior Analysis

Torsion also plays an important role in the overall stability of the CDLT. To examine its mechanical response and geometric nonlinearity under pure torsion, tests were carried out as described in Section 2.2. Figure 10 compares the experimentally observed torsional buckling with numerical predictions. The close agreement between the measured deformation modes and the FE results shows that the model can accurately capture both the onset and progression of torsional buckling. The torque–twist curve presents two stages: a linear pre-buckling regime and a nonlinear post-buckling regime. In the linear range, torque increases almost proportionally with twist, which reflects the shear-dominated response of closed thin-walled sections. As the twist continues to increase, the torque reaches a critical peak at the point of instability and then gradually decreases. The FE model predicts a slightly higher stiffness than the experiments, mainly because it assumes ideal geometry, uniform

thickness, and purely elastic behavior, without accounting for imperfections in the actual specimen. Even so, the experimental and simulated torque–twist responses agree well overall. To further examine the stress development under torsion, the stress distributions in each layer at the maximum torque were extracted, as shown in Figure 11. The structure reached peak torque at a torsional angle of 0.46 rad, beyond which local buckling began. Under this critical condition, significant stress concentration was observed in the adhesive interface region at the mid-section of the tube. Stress contour plots from the FE analysis for different layers indicate that the inner three layers exhibit nearly identical, relatively low stress levels. In comparison, the outermost two layers bear the highest stress intensities.

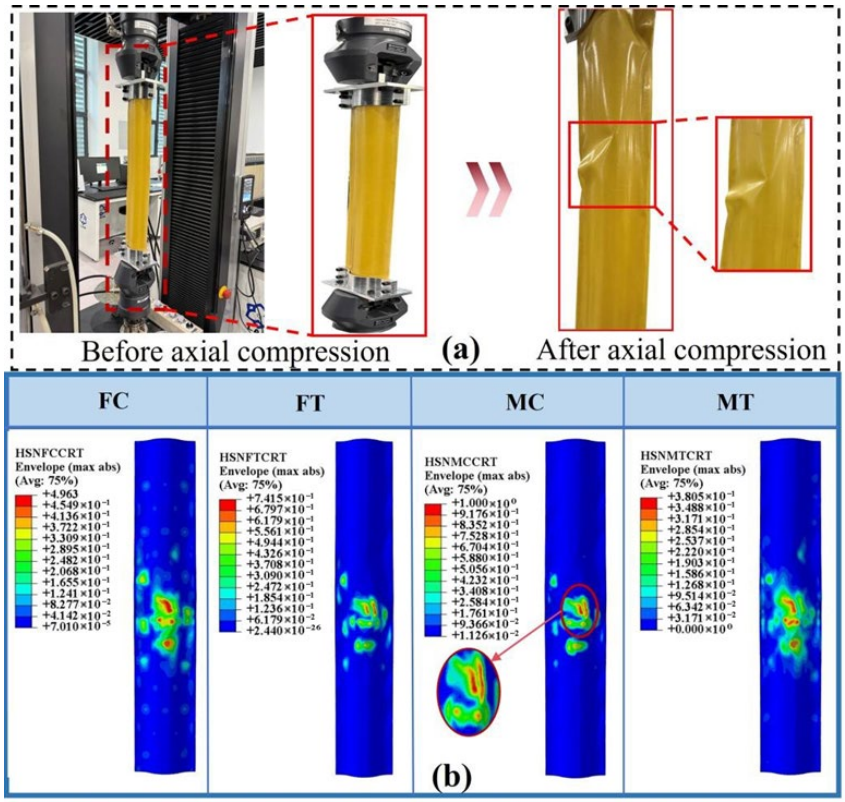


Figure 9. (**a**) Buckling failure process under axial compression; (**b**) FE contour plot based on Hashin criteria, showing axial compression damage.

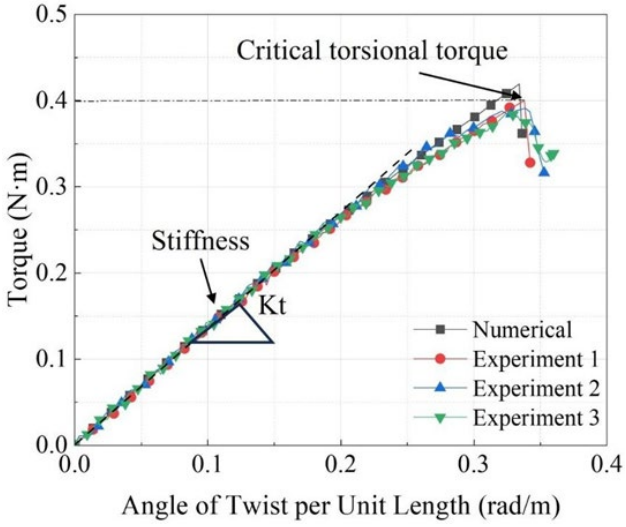


Figure 10. Comparison of numerical and experimental torque–twist relationships.

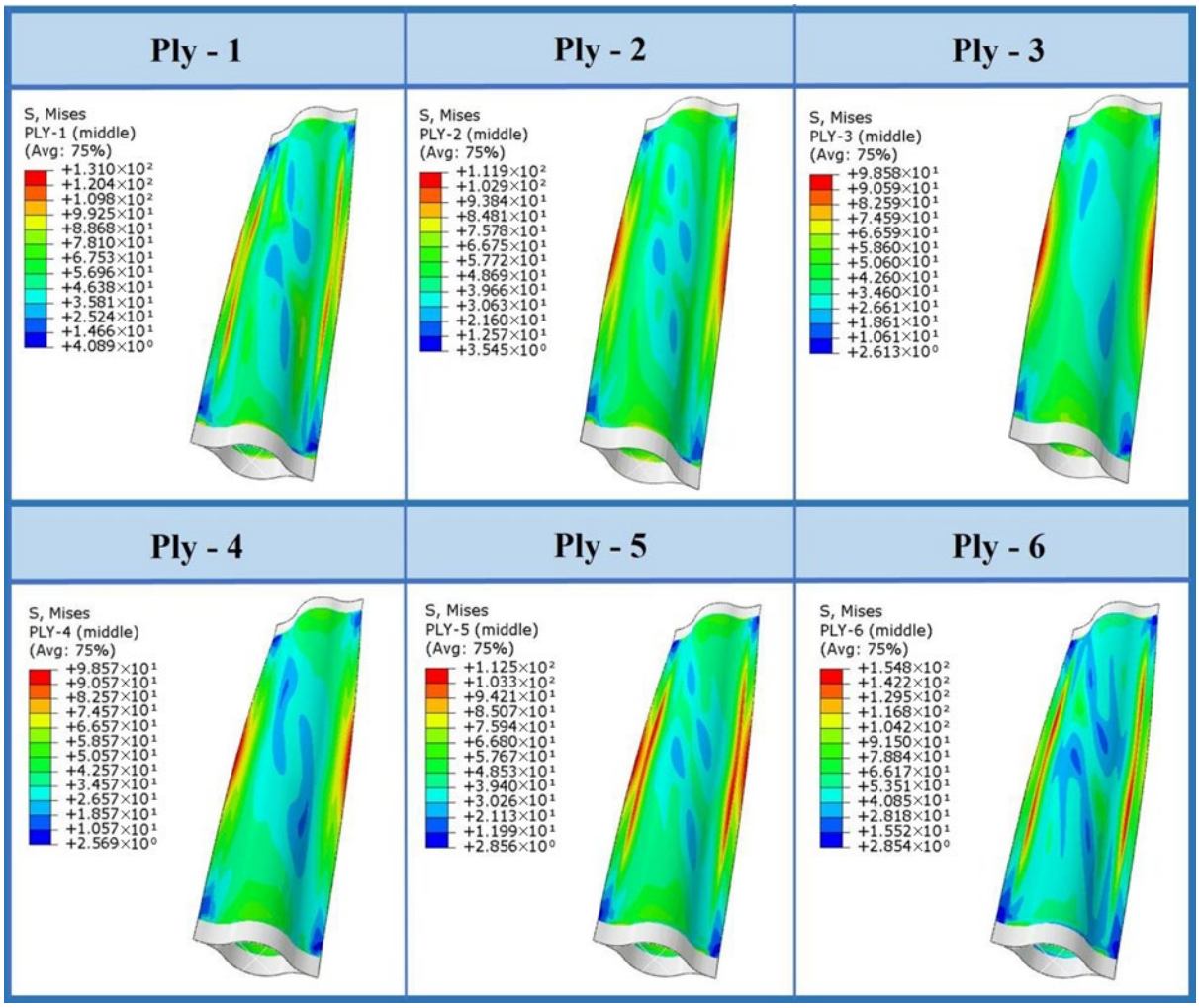


Figure 11. Simulation of CDLT torsional deformation evolution at maximum torsional radius.

4. Result and Discussion

4.1. Study of Parameters of Axial Compression and Torsion

Under external loading, the CDLT may experience bending or local buckling. Its geometry and material properties govern overall stability. This study systematically analyzed the effects of layer number, layer thickness, and layer angle on the axial compression and torsional stability of CDLTs. Displacement–load curves of CDLT specimens in different layers are shown in Figure 12a and Table 2. As shown in the figure, when the total layer thickness is fixed at 0.72 mm, progressively increasing the number of layers in the CDLT structure from 4 to 8 layers produces nearly identical load–displacement curves under axial compression. This result indicates that, under constant thickness, increasing the number of layers discretizes the thickness-direction stiffness distribution without altering the structure's effective in-plane stiffness or bending stiffness. As a result, the critical buckling load and the maximum compression displacement show almost no variation. From a design standpoint, this means that reducing the number of plies while keeping the total thickness constant preserves the mechanical performance and also simplifies manufacturing.

In contrast, layer thickness has a much stronger effect on the critical buckling capacity. A nonlinear buckling analysis was performed on a six-layer CDLT with thicknesses ranging from 0.48 mm to 0.96 mm. As shown in Table 3 and Figure 12b, the critical load increases markedly—from 911.5 N at 0.48 mm to 3746.0 N at 0.96 mm, a 4.11-fold rise. The results show that increasing the thickness of each ply improves overall stiffness and resistance to

local buckling, thereby increasing the axial buckling capacity of the CDLT. By examining the slope of the load–displacement curves, the corresponding displacement–stiffness trend was obtained (Figure 12c). The stiffness drops as deformation grows, a consequence of accumulated local bending and shell deformation, indicating that the load-carrying ability decreases significantly before global buckling occurs.

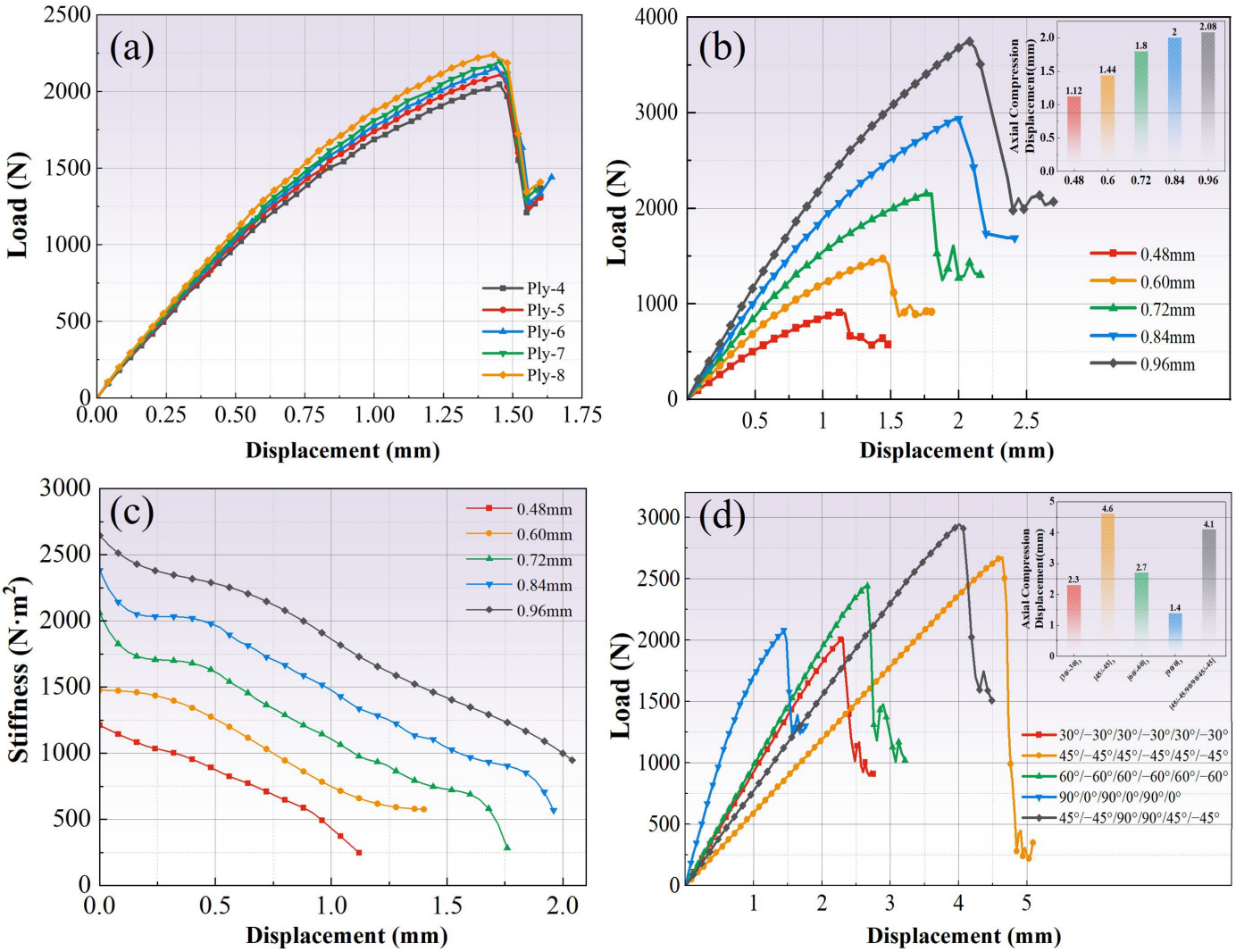


Figure 12. Displacement–load and stiffness curves of CDLTs under axial compression at different parameters: (**a**) load–displacement curves in different numbers of ply layup; (**b**) load–displacement curves in different thicknesses; (**c**) stiffness–displacement curves in different thicknesses; (**d**) load–displacement curves at different angles of ply layup.

Table 2. Linear and nonlinear critical buckling loads in various numbers of ply layup.

Number	Linear (N)	Nonlinear (N)
4	2783.2	2046.5
5	3251.2	2111.2
6	3059.8	2154.8
7	3170.1	2183.4
8	3493.9	2239.7

The influence of the ply angle was also examined at a fixed total thickness of 0.72 mm using five stacking sequences: $[30°/-30°]_3$, $[45°/-45°]_3$, $[60°/-60°]_3$, $[90°/0°]_3$, and $[45°/-45°/90°/90°/45°/-45°]$. The load–displacement curves for each configuration are

shown in Figure 12d and Table 4, and the corresponding nonlinear critical loads and peak displacements are listed in Table 4. The critical load rises from 2015.3 N for $[30°/-30°]_3$ to 2673.6 N for $[45°/-45°]_3$, then decreases to 2154.8 N for $[90°/0°]_3$. Introducing a 90° ply within the ±45° stack further increases the critical load to 2910.2 N—1.44 times the minimum value. Specimens containing 90° plies between ±45° layers show the best axial compression performance. Among all configurations, the $[45°/-45°/90°/90°/45°/-45°]$ layup achieves the highest buckling load. This improvement comes from the combined effect of the ±45° layers, which enhance shear coupling, and the 90° layers, which provide strong axial reinforcement, resulting in improved post-buckling stability.

Table 3. Near and nonlinear critical buckling loads for various thicknesses of six plies.

Thickness (mm)	Linear (N)	Nonlinear (N)
0.48	1367.3	911.5
0.60	2154.2	1475.5
0.72	3059.8	2154.8
0.84	4698.8	2936.8
0.96	5731.3	3746.0

Table 4. Linear and nonlinear critical buckling loads for various angles of ply layup.

Angles	Linear (N)	Nonlinear (N)
$30°/-30°/30°/-30°/30°/-30°$	3043.1	2015.3
$45°/-45°/45°/-45°/45°/-45°$	4277.7	2673.6
$60°/-60°/60°/-60°/60°/-60°$	3212.4	2379.6
$90°/0°/90°/0°/90°/0°$	3059.8	2154.8
$45°/-45°/90°/90°/45°/-45°$	4539.9	2910.2

Figure 13 shows the torque–twist and stiffness curves of CDLTs with different parameters. As shown in Figure 13a and Table 5, when the total laminate thickness is fixed at 0.72 mm, increasing the number of layers from four to eight produces nearly identical torque–twist curves. This trend is consistent with the axial compression results, indicating that simply changing the number of layers has little effect on torsional performance. When other parameters are fixed, increasing the layer number reduces the thickness of each layer, but the overall stiffness characteristics remain almost unchanged, so it has only a slight effect on torsional stiffness. In contrast, the total laminate thickness has a much stronger influence on torsional behavior. As listed in Table 6 and shown in Figure 13b,d, increasing the thickness from 0.48 mm to 0.96 mm increases the maximum critical torque from 0.248 N·m to 0.599 N·m, while the torsional stiffness nearly doubles from 0.806 N·m^2 to 1.813 N·m^2. This is mainly due to the significant increase in the equivalent shear stiffness of CDLT with increasing thickness.

Table 5. Linear and nonlinear critical buckling loads for varying numbers of ply layup.

Numbers	Torque (N·m)	Stiffness (N·m^2)
4	0.399	1.250
5	0.408	1.274
6	0.418	1.301
7	0.427	1.331
8	0.442	1.378

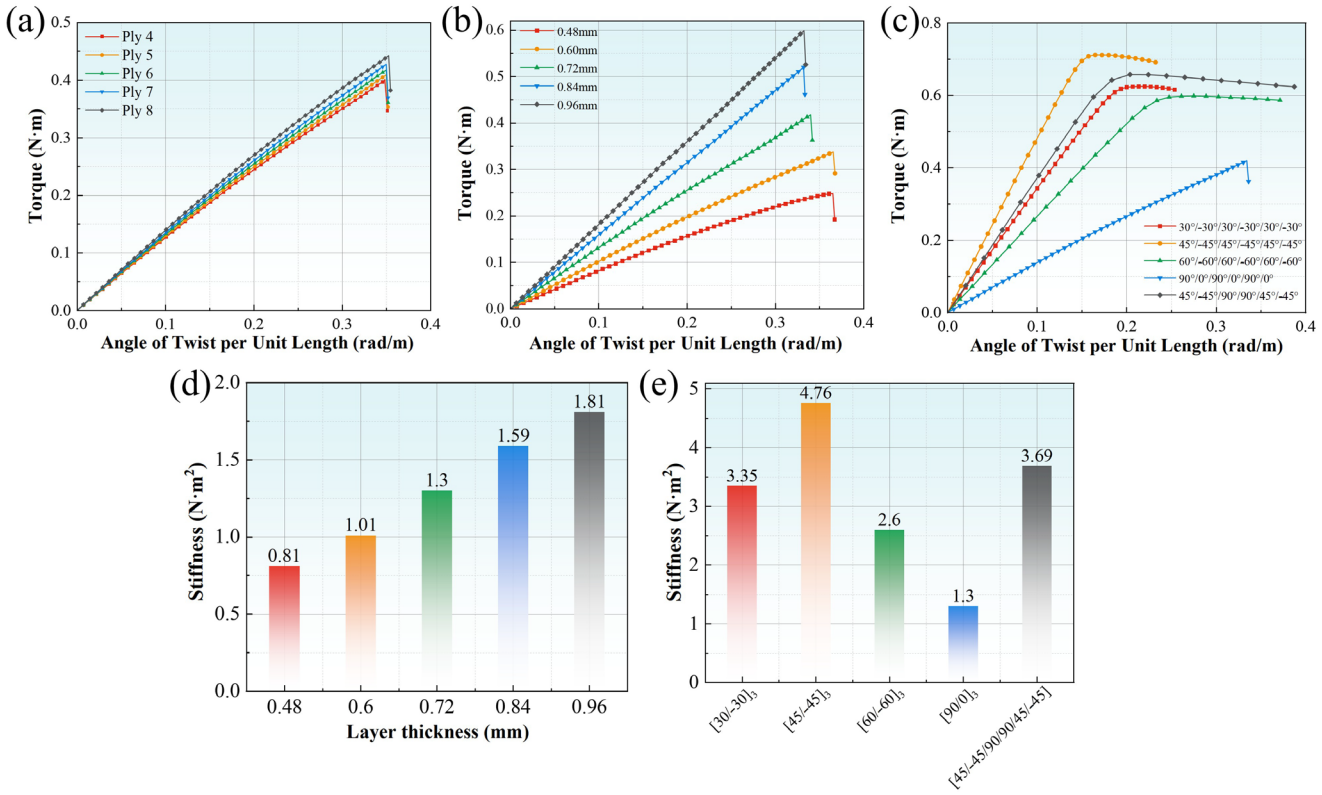


Figure 13. Torque–twist and stiffness curves of CDLT torsion under different parameters: (**a**) torque–twist curves for different numbers of ply layup; (**b**) torque–twist curves for different thicknesses; (**c**) torque–twist curves for different angles of ply layup; (**d**) torsional stiffness for different thicknesses; (**e**) torsional stiffness for different angles of ply layup.

Table 6. Linear and nonlinear critical buckling loads for varying thicknesses of six plies.

Thickness (mm)	Torque (N·m)	Stiffness (N·m^2)
0.48	0.248	0.806
0.60	0.343	1.008
0.72	0.418	1.301
0.84	0.520	1.589
0.96	0.599	1.813

The effects of ply orientation on torsional behavior were also examined. As shown in Table 7 and Figure 13c,e, the ply angle strongly affects both the maximum critical torque and torsional stiffness. These values increase as the ply angle approaches ±45°, reaching their highest levels for the $[45°/-45°]_3$ laminate, which achieves a maximum critical torque of 0.712 N·m and a torsional stiffness of 4.760 N·m^2. Unlike the trend observed in axial compression, the $[45°/-45°/90°/90°/45°/-45°]$ configuration does not show improved torsional performance. This difference arises because torsion is governed mainly by in-plane shear strain, which is best resisted by fibers aligned at ±45°. Although the 90° plies benefit axial strength, they reduce the fraction of fibers aligned with the primary shear direction, lowering the laminate's shear efficiency and overall torsional rigidity.

Overall, the results show that both the stacking sequence and the total laminate thickness play essential roles in determining the load-bearing capacity of the CDLT. Among the configurations tested, the $[45°/-45°/90°/90°/45°/-45°]$ layup offers the best balance, with the 90° layers providing higher axial strength and the ±45° layers improving shear resistance. Increasing the laminate thickness also leads to a steady increase in load-bearing

capacity, but overly thick laminates significantly reduce stowability. This makes it necessary to experimentally assess the coiling performance of CDLTs with different thicknesses.

Table 7. Linear and nonlinear critical buckling loads for varying angles of ply layup.

Angles	Torque (N·m)	Stiffness (N·m^2)
30°/−30°/30°/−30°/30°/−30°	0.623	3.349
45°/−45°/45°/−45°/45°/−45°	0.712	4.760
60°/−60°/60°/−60°/60°/−60°	0.596	2.596
90°/0°/90°/0°/90°/0°	0.418	1.301
45°/−45°/90°/90°/45°/−45°	0.658	3.692

4.2. Coiling Mechanical Property Analysis

This section verifies the stowability of CDLTs through experiments and FE simulations. A dedicated experimental platform was constructed for the CDLT coiling test. The apparatus comprises three subsystems: a storage system, a drive system, and a data acquisition system (Figure 14a). An FE model was established based on experimental loads and boundary conditions (Figure 14b). The CDLT was modeled as three-dimensional deformable shells using four-node, simplified quadrilateral (S4R) elements.

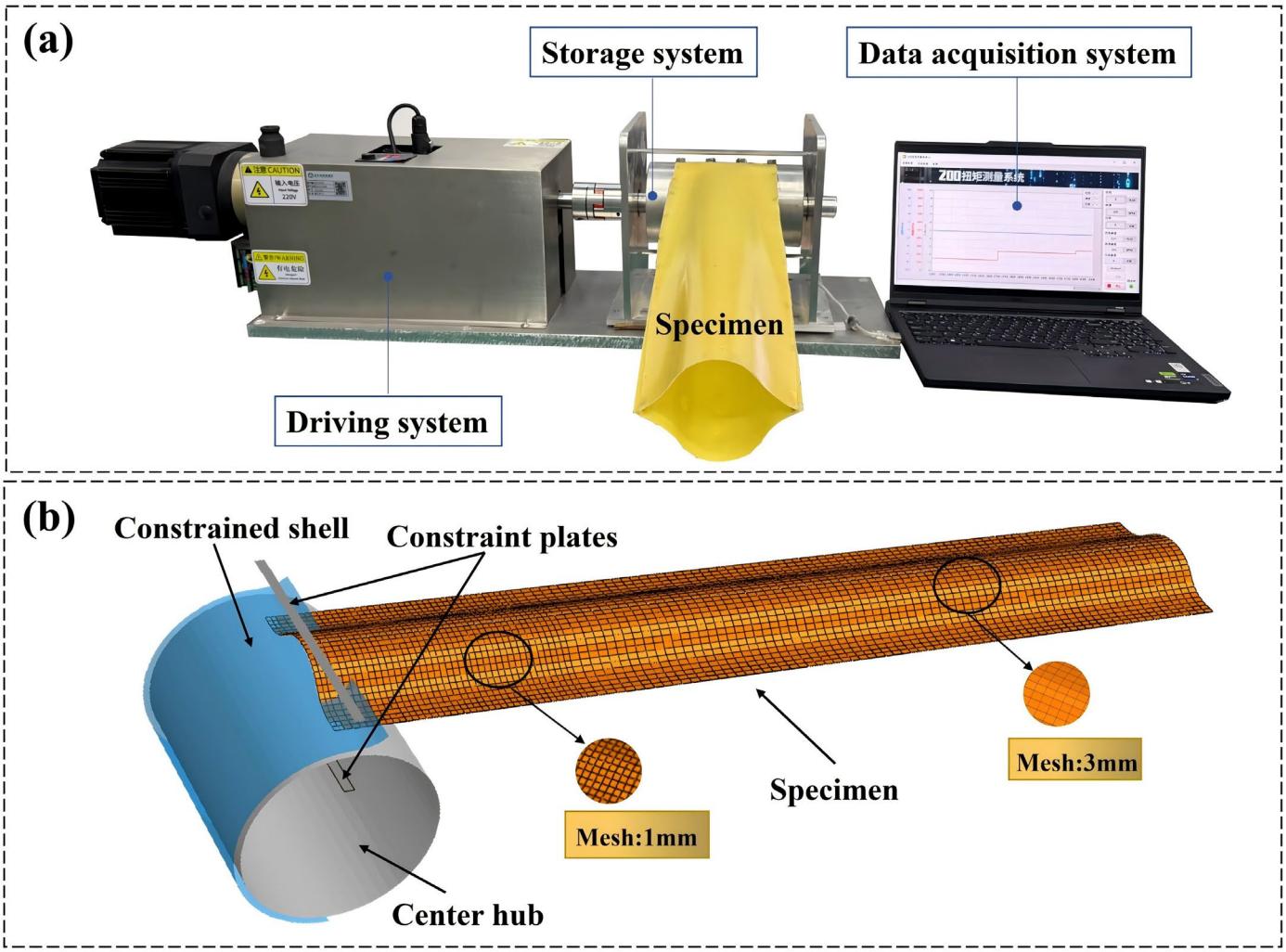


Figure 14. (**a**) Coiling deformation processes of the CDLT through experiments and (**b**) FE model and mesh density for coiling.

The two overlapping boundaries of the CDLT were connected using COH3D8 adhesive elements, with the adhesive layer modeled as an eight-node three-dimensional adhesive interface [14]. The energy storage components were modeled as discrete rigid bodies using R3D4 elements. The analysis employed an explicit dynamic integration scheme. The specific simulation process is detailed in the Supporting Materials S2.

Figure 15 illustrates the CDLTs coiling process obtained from experiments and quasi-static FE simulations. One end of the CDLTs was flattened and bolted to the roller, with a data acquisition system continuously recording torque and angular displacement. The simulated deformation closely matches experimental results conducted at room temperature and constant rotational speed. FE results indicate stable overall deformation during coiling, with peak stresses concentrated near the fixed end, where the shell contacts the central roller. Local stresses in the lateral arc region exceed those in the central arc region, primarily due to increased local curvature and bending effects induced by shell edge contact. Figure 16a shows the coiling torque derived from FE simulations and experimental measurements. The results indicate good agreement between numerical and experimental data, with both obtaining fluctuating yet generally stable torque curves. The average coiling torque reaches 1.5 N·m. The slightly higher simulation results may result from the idealized assumption of frictionless motion at the boom–roller interface.

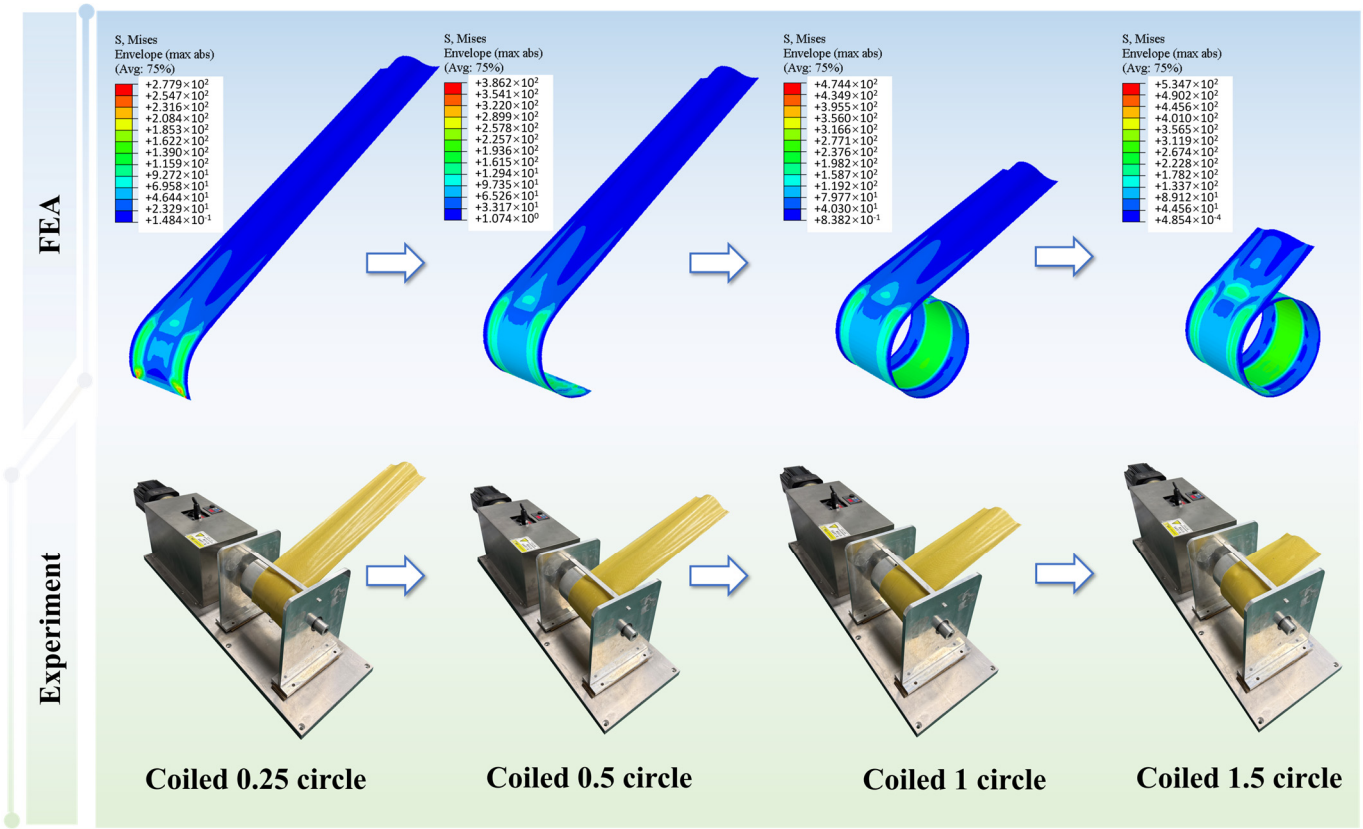


Figure 15. Coiling deformation processes of the CDLT determined during experiments and numerical simulation.

Figure 16b presents the coiling torque of CDLT with the same layer sequence [45°/−45°/90°/90°/45°/−45°] but different thicknesses ranging from 0.48 mm to 0.96 mm. When the thickness increased to 0.72 mm, the coiling torque increased only slightly from 1.37 N·m to 1.50 N·m. However, the coiling torque increased markedly with increasing laminate thickness, reaching 1.98 N·m at 0.84 mm and further increasing to 2.61 N·m at 0.96 mm. Thus, laminates with a thickness of approximately 0.72 mm achieve an optimal

balance, ensuring both unfolding stability and the flexibility required for efficient coiling. To further verify the coiling performance of Kevlar CDLT, the CFRP CDLTs commonly used in current aerospace deployable structures are compared. Both tubes adopt identical lenticular cross-sectional dimensions, as shown in Section 2.1, fully consistent boundary conditions, and a total laminate thickness of 0.72 mm, with the stacking sequence set as [45°/−45°/90°/90°/45°/−45°]. The only variable between them is the constitutive material properties. All CFRP material parameters are taken from a single reference source and compiled together with Kevlar properties in Table 8. The comparison results in Figure 16c show that CFRP specimens consistently exhibit higher coiling torque than Kevlar specimens, with peak torques of 2.70 N·m to 3.25 N·m. Under comparable conditions, Kevlar specimens reduce torque by at least 48% compared to CFRP specimens.

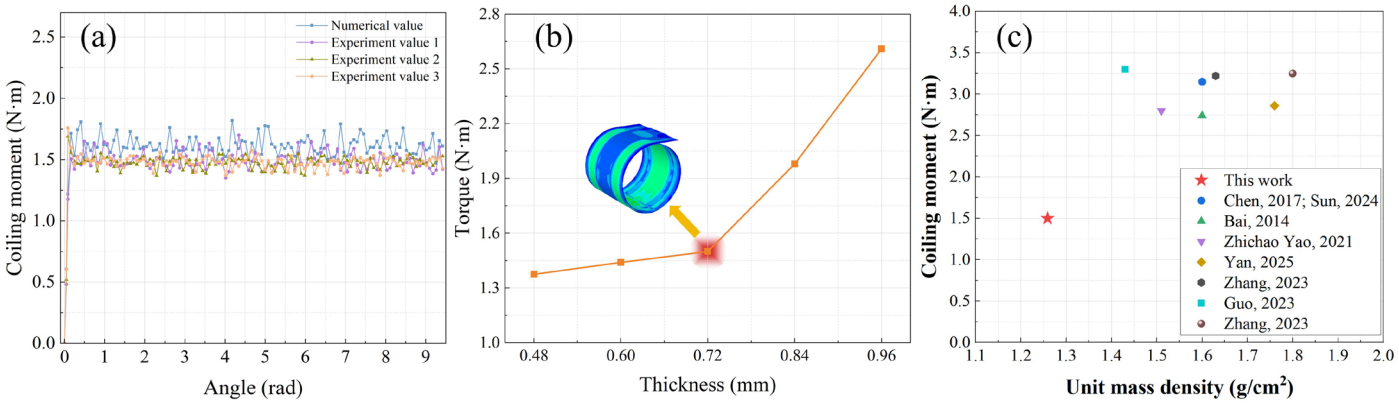


Figure 16. Coiling responses of CDLTs: (**a**) coiling moment from numerical and experimental results; (**b**) coiling torque at different thicknesses; (**c**) comparison of coiling performance under different material parameters [7,14,36–40].

Table 8. Material properties of Kevlar fiber and the referenced carbon fiber prepreg.

Number	Fiber Type	E_1 (GPa)	E_2 (GPa)	v_{12} (GPa)	G_{12} (GPa)	Density (g/cm^3)	Refs.
1	Kevlar/9788	20.5	6.0	0.21	0.77	1.26	[35]
2	T300/Epoxy	93.69	4.51	0.30	2.38	1.76	[36]
3	T300/Epoxy	82.30	6.77	3.50	0.33	1.51	[37]
4	T300/Epoxy	137.99	8.71	0.32	3.50	1.43	[38]
5	T300/Epoxy	130	10	0.3	4.4	1.8	[39]
6	T700/Epoxy	129	3.1	0.32	6.1	1.63	[39]
7	T300/5228	126	7.2	0.3	3.6	1.6	[7,14]
8	T300/5228A	80.08	6.67	0.34	2.93	1.6	[40]

5. Conclusions

The buckling behavior of Kevlar CDLTs under axial compression and torsion was experimentally and numerically studied in a combined manner. The key findings are as follows:

(1) Experiments and numerical simulations for axial compression revealed similar behavior, and both confirmed that the CDLT follows an initial linear elastic behavior until a critical load, where it buckles, causing a sharp reduction in compressive load and stiffness. Stress analysis indicated that during compressive buckling, stresses are mainly concentrated in the central arc section, while stresses in the flange region remained at a low level throughout the entire loading process. Validation of the

damage evolution further confirmed that matrix compression failure is the prevailing post-buckling failure mechanism.

(2) Custom platform and FEA-based torsion tests revealed that the torque–twist response was initially linear, but dropped sharply at the peak torque due to local buckling and global instability. The stress analysis also showed that the highest stresses were observed for the outermost layers, and there were more uniform lower stress levels on intermediate layers.

(3) The parametric analysis reveals that the total thickness and layer orientation play a dominant role in the load-bearing capacity of CDLTs, and adding layers while maintaining constant thickness had a limited effect on further improvement. The layup $[45°/-45°/90°/90°/45°/-45°]$ was found to significantly increase load-bearing capacity. While increasing the laminate thickness enhances the CDLT's load-bearing capacity, an overly thick design reduces its stowability.

(4) The effects of laminate thickness on coiling torque were investigated using a custom platform for coiling test and FE calculations. Experiments were in good agreement with simulations, and the coiling torque was found to increase with thickness. Notably, torque rose slowly for thicknesses below 0.72 mm but increased sharply beyond this point due to stiffness-dominated resistance. Consequently, a thickness of 0.72 mm was found to be ideal, as it was strong enough load-bearing-wise and minimized coiling torque.

Overall, this study has preliminarily verified the load-bearing potential of the novel Kevlar CDLT and its stowability, which will help inform the design and optimization of future space-lightweight, flexible, deployable structures. Further studies will focus on the thermodynamic response in orbital environments, leveraging deployment experiments and high-fidelity numerical simulations to enhance its suitability for long-term space applications.

Supplementary Materials: The following supporting information can be downloaded at: https://www.mdpi.com/article/10.3390/eng7020096/s1, S1: Sensitivity analysis of mesh density; Table S1: Sensitivity analysis of mesh density for FE modes; S2: Coiling FE simulation process.

Author Contributions: Investigation: X.W. (Xinrui Wang) and J.S.; methodology: X.W. (Xinrui Wang); software: X.W. (Xinrui Wang); formal analysis: X.W. (Xinrui Wang); validation: X.W. (Xinrui Wang) and J.S.; writing—original draft: X.W. (Xinrui Wang); data curation: J.S.; investigation, methodology: X.W. (Xingjian Wang); supervision: J.Y.; writing—review and editing: Q.Z.; supervision: Q.Z; conceptualization: J.S.; supervision: J.S.; resources: J.S.; funding acquisition: J.S.; project administration: J.S.; writing—review and editing: J.S. All authors have read and agreed to the published version of the manuscript.

Funding: This work was supported by the National Key R&D Program of China (2021YFF0500103), the pre-production and industrialization projects of Scientific and Technological Achievements of Jilin University (23GNZ24), and the Program for the Central University Youth Innovation Team (419021423505).

Data Availability Statement: The original contributions presented in this study are included in the article/Supplementary Materials. Further inquiries can be directed to the corresponding author.

Conflicts of Interest: The authors declare that they have no known competing financial interests or personal relationships that could have appeared to influence the work reported in this paper.

References

1. Galhofo, D.; Silvestre, N.; de Deus, A.M.; Reis, L.; Duarte, A.P.C.; Carvalho, R. Structural behaviour of pre-tensioned solar sails. *Thin-Walled Struct.* **2022**, *181*, 110007. [CrossRef]
2. Gibney, E. CubeSats set for deep space—If they can hitch a ride. *Nature* **2016**, *535*, 19–20. [CrossRef] [PubMed]

3. Liddle, J.D.; Holt, A.P.; Jason, S.J.; O'Donnell, K.A.; Stevens, E.J. Space science with CubeSats and nanosatellites. *Nat. Astron.* **2020**, *4*, 1026–1030. [CrossRef]
4. Leclerc, C.; Pellegrino, S. Nonlinear elastic buckling of ultra-thin coilable booms. *Int. J. Solids Struct.* **2020**, *203*, 46–56. [CrossRef]
5. Bessa, M.A.; Pellegrino, S. Design of ultra-thin shell structures in the stochastic post-buckling range using Bayesian machine learning and optimization. *Int. J. Solids Struct.* **2018**, *139–140*, 174–188. [CrossRef]
6. Kajihara, S.; Yamashita, S.; Sunaga, Y.; Yokozeki, T.; Watanabe, A.; Iwahori, Y. Deformation behavior of CFRP bistable open-section cylindrical boom for lunar deployable structure. *Thin-Walled Struct.* **2025**, *216*, 113651. [CrossRef]
7. Chen, W.; Fang, G.; Hu, Y. An experimental and numerical study of flattening and wrapping process of deployable composite thin-walled lenticular tubes. *Thin-Walled Struct.* **2017**, *111*, 38–47. [CrossRef]
8. Schultz, M.R.; Hulse, M.J.; Keller, P.N.; Turse, D. Neutrally stable behavior in fiber-reinforced composite tape springs. *Compos. Part A Appl. Sci. Manuf.* **2008**, *39*, 1012–1017. [CrossRef]
9. Yang, L.; Tan, H.; Cao, Z. Modeling and analysis of the ploy region of bistable composite cylindrical shells. *Compos. Struct.* **2018**, *192*, 347–354. [CrossRef]
10. Wang, F.; Zhang, J.; Wang, S. Investigation on flow and heat transfer characteristics in rectangular channel with drop-shaped pin fins. *Propuls. Power Res.* **2012**, *1*, 64–70. [CrossRef]
11. Nguyen, L.; Medina, K.; McConnel, Z.; Lake, M.S. Solar Cruiser TRAC boom development. In *AIAA SCITECH 2023 Forum*; American Institute of Aeronautics and Astronautics: Reston, VA, USA, 2023.
12. Yang, H.; Guo, H.; Liu, R.; Wang, S.; Liu, Y. Coiling and deploying dynamic optimization of a C-cross section thin-walled composite deployable boom. *Struct. Multidiscip. Optim.* **2020**, *61*, 1731–1738. [CrossRef]
13. Chang, Z.; Zhao, P.; Zhang, Z.; Zou, G.; Zhao, P.; Wu, C. Damage analysis of deployable thin-walled composite shell structure during coiling up. *Thin-Walled Struct.* **2024**, *195*, 111395. [CrossRef]
14. Sun, J.; Han, Q.; Cheng, X.; Shi, H.; Ding, R.; Shi, M.; Liu, C. A data-driven computational optimization framework for designing thin-walled lenticular deployable composite boom with optimal load-bearing and folding capabilities. *Thin-Walled Struct.* **2024**, *203*, 112244. [CrossRef]
15. Leipold, M.; Eiden, M.; Garner, C.; Herbeck, L.; Kassing, D.; Niederstadt, T.; Krüger, T.; Pagel, G.; Rezazad, M.; Rozemeijer, H.; et al. Solar sail technology development and demonstration. *Acta Astronaut.* **2003**, *52*, 317–326. [CrossRef]
16. Puig, L.; Barton, A.; Rando, N. A review on large deployable structures for astrophysics missions. *Acta Astronaut.* **2010**, *67*, 12–26. [CrossRef]
17. Gan, W.W.; Pellegrino, S. Numerical Approach to the Kinematic Analysis of Deployable Structures Forming a Closed Loop. *Proc. Inst. Mech. Eng. Part C J. Mech. Eng. Sci.* **2006**, *220*, 1045–1056. [CrossRef]
18. Nassehpour, S.; Kwan, A.S.K. New concepts in large deployable parabolic solid reflectors. In Proceedings of the 6th AECEF Symposium on Civil Engineering Education in Changing Europe, Vilnius, Lithuania, 28–30 May 2008; pp. 162–171.
19. Seffen, K.A.; You, Z. Pellegrino, Folding and deployment of curved tape springs. *Int. J. Mech. Sci.* **2000**, *42*, 2055–2073. [CrossRef]
20. Wang, B.; Zhu, J.; Zhong, S.; Liang, W.; Guan, C. Space deployable mechanics: A review of structures and smart driving. *Mater. Des.* **2024**, *237*, 112557. [CrossRef]
21. Lappas, V.; Adeli, N.; Visagie, L.; Fernandez, J.; Theodorou, T.; Steyn, W.; Perren, M. CubeSail: A low cost CubeSat based solar sail demonstration mission. *Adv. Space Res.* **2011**, *48*, 1890–1901. [CrossRef]
22. Geppert, U.; Biering, B.; Lura, F.; Block, J.; Straubel, M.; Reinhard, R. The 3-step DLR–ESA Gossamer road to solar sailing. *Adv. Space Res.* **2011**, *48*, 1695–1701. [CrossRef]
23. Zhang, Z.; Li, Y.; Yu, X.; Li, X.; Wu, H.; Wu, H.; Jiang, S.; Chai, G. Bistable morphing composite structures: A review. *Thin-Walled Struct.* **2019**, *142*, 74–97. [CrossRef]
24. Sun, J.; Wang, X.; Cheng, X.; Shi, H.; Ding, R.; Han, Q.; Liu, C. Prediction of nonlinear mechanical behaviour of the corrugated flexible composite skin for morphing wing via PCA-enhanced deep learning method. *Aerosp. Sci. Technol.* **2026**, *168*, 111018. [CrossRef]
25. Block, J.; Straubel, M.; Wiedemann, M. Ultralight deployable booms for solar sails and other large gossamer structures in space. *Acta Astronaut.* **2011**, *68*, 984–992. [CrossRef]
26. Tanaka, H. Design optimization studies for large-scale contoured beam deployable satellite antennas. *Acta Astronaut.* **2006**, *58*, 443–451. [CrossRef]
27. Soykasap, O.; Watt, A.M.; Pellegrino, S. New Deployable Reflector Concept. In Proceedings of the 45th AIAA/ASME/ASCE/AHS/ASC Structures, Structural Dynamics & Materials Conference, Palm Springs, CA, USA, 19–22 April 2004.
28. Palmeri, F.; Laurenzi, S. Neural Network-Based Surrogate Modeling for Buckling Performance Optimization of Lightweight-Composite Collapsible Tubular Masts. *Biomimetics* **2024**, *9*, 494. [CrossRef]
29. Sun, J.; Cheng, X.; Wang, X.; Shi, H.; Ding, R.; Han, Q.; Liu, C. Rapidly predicting curing process-induced deformation of the thin-walled Omega-shaped composite parts using a deep learning method. *Thin-Walled Struct.* **2025**, *217*, 113906. [CrossRef]

30. Hu, Y.; Chen, W.; Li, R.; Fang, G. Mechanical characteristics of deployable composite thin-walled lenticular tubes. *Compos. Struct.* **2016**, *153*, 601–613. [CrossRef]
31. Ma, X.; An, N.; Cong, Q.; Bai, J.-B.; Wu, M.; Xu, Y.; Zhou, J.; Zhang, D.; Zhang, T.; Guo, R.; et al. Design, modeling, and manufacturing of high strain composites for space deployable structures. *Commun. Eng.* **2024**, *3*, 78. [CrossRef]
32. Seay, C.W.; Mulcahy, K.A.; Hall, M.S.; Clements, J.A.; Pretko, J.; Christiansen, E.L.; Davis, B.A.; Cowardin, H. *Cowardin, The Next Generation of Kevlar Fiber for Improved Micrometeoroid and Orbital Debris Protection*; NASA: Washington, DC, USA, 2023.
33. Quinn, H.; Roussel-Dupre, D.; Caffrey, M.; Graham, P.; Wirthlin, M.; Morgan, K.; Salazar, A.; Nelson, T.; Howes, W.; Johnson, E.; et al. The Cibola Flight Experiment. *ACM Trans. Reconfig. Technol. Syst.* **2015**, *8*, 3. [CrossRef]
34. Schenk, M.; Viquerat, A.D.; Seffen, K.A.; Guest, S.D. Review of Inflatable Booms for Deployable Space Structures: Packing and Rigidization. *J. Spacecr. Rocket.* **2014**, *51*, 762–778. [CrossRef]
35. Guo, G.; Alam, S.; Peel, L.D. An investigation of deformation and failure mechanisms of fiber-reinforced composites in layered composite armor. *Compos. Struct.* **2022**, *281*, 115125. [CrossRef]
36. Yan, Z.; Wu, M.; Xiang, P. An energy method to predict the peak moment of CFRP lenticular booms under pure bending. *Aerosp. Sci. Technol.* **2025**, *158*, 109921. [CrossRef]
37. Yao, Z.; Li, D.; Zhu, S.; Zhou, L. Analysis of Buckling Characteristics and Parameter Influence of Composite Thin-walled Lenticular Boom Structures. *E3S Web Conf.* **2021**, *233*, 04009. [CrossRef]
38. Guo, R.; Jin, X.; Jia, Q.; Ma, X.; An, N.; Zhou, J. Folding, stowage, and deployment of composite thin-walled lenticular tubes. *Acta Astronaut.* **2023**, *213*, 567–577. [CrossRef]
39. Zhang, Z.; Guo, X.; Pan, B.; Sun, M.; Zhang, G.; Chai, H.; Wu, H.; Jiang, S. Experimental study and numerical simulation of load-bearing/coiling characteristics of thin-walled lenticular composite booms. *Compos. Struct.* **2023**, *324*, 117515. [CrossRef]
40. Bai, J.; Xiong, J. Temperature effect on buckling properties of ultra-thin-walled lenticular collapsible composite tube subjected to axial compression. *Chin. J. Aeronaut.* **2014**, *27*, 1312–1317. [CrossRef]

Disclaimer/Publisher's Note: The statements, opinions and data contained in all publications are solely those of the individual author(s) and contributor(s) and not of MDPI and/or the editor(s). MDPI and/or the editor(s) disclaim responsibility for any injury to people or property resulting from any ideas, methods, instructions or products referred to in the content.